ADVANCED MATERIALS
www.advmat.de

Solvent Annealing of Perovskite-Induced Crystal Growth for Photovoltaic-Device Efficiency Enhancement

*Zhengguo Xiao, Qingfeng Dong, Cheng Bi, Yuchuan Shao, Yongbo Yuan, and Jinsong Huang**

Material crystallinity is paramount in determining the electronic properties in both organic and inorganic electronic materials and the performance of electronic devices.[1–4] Thermal annealing is the most broadly applied technique to increase the crystallinity of materials, especially thin films, because of its simplicity. Complementary to thermal-annealing, solvent-annealing, where solvent vapor is introduced during the crystallization of the bulk or thin film materials,[2,3] has been found to be an effective method to increase the crystallinity of some very specific organic semiconductors; however, it has never been demonstrated in inorganic semiconductors. Here we show that solvent-annealing can be applied to a new family of organic–inorganic hybrid materials—organometal trihalide perovskites—to increase the crystallinity and grain size.

Methylamonium lead trihalide perovskites (CH_3NH_3)PbX_3, where X is the halogen I, Br or Cl) are emerging as a new generation of solution-processable, low-cost photovoltaic materials which are abundant in nature.[5–19] High power conversion efficiencies of around 15% have been achieved in both mesoporous structures and planar heterojunction (PHJ) structure devices, using either spin-casting or thermal-evaporation deposition methods.[5–19] One issue with solution-processed perovskite thin films is that the polycrystalline films have a relatively small grain size of a couple of hundred nanometers (nm) due to the quick reaction of lead iodide (PbI_2) and methylamonium iodide (MAI) and the quick crystallization of these perovskite materials.[20] Most of the best-performing devices have a perovskite thickness of around 300 nm.[4,6] Perovskite film that is thicker, up to 1 μm, is desirable so that sunlight can be absorbed more completely, especially in the red to infrared range. Another merit of having a thicker perovskite film is that the device's manufacturing yield can be increased, which is especially important in larger scale manufacturing using high-throughput methods such as printing, blade coating, or gravure coating. This is because a thicker film reduces the chance of leakage spot formation, the importance of which has already been broadly recognized by the organic photovoltaic field.[21] Thermal annealing could be used to increase the grain size and crystallinity of these perovskites to some extent; however, the margin is very small, as shown in this work. Moreover, high-temperature thermal annealing, or even low-temperature thermal annealing for long periods, decomposes the perovskite films and so decreases the device efficiency.[22,23]

In this manuscript, we report that solvent annealing effectively increases the crystallinity and grain size of $CH_3NH_3PbI_3$ film. The average grain size of the solvent-annealed trihalide $CH_3NH_3PbI_3$ films increased to 1 μm, which is comparable to the film thickness, while the maximum grain size in thermal annealed films was only around 260 nm. Solvent annealing dramatically improved the electronic properties of the perovskite films. The best-performing device with planar structure had an efficiency of 15.6% under air mass global (AM 1.5G) spectrum illumination with a perovskite thickness of 630 nm; the efficiency dropped only slightly to 14.5% when the pervoskite thickness increased to 1 μm.

The perovskite films were fabricated by the interdiffusion of spun stacking of double layers of PbI_2 and MAI, as illustrated in **Figure 1**a.[24] PbI_2 and MAI were first dissolved in dimethylformamide (DMF) and 2-propanol, respectively, as precursor solutions at varied concentration. The precursors were then spun onto poly(3,4-ethylenedioxythiophene) poly(styrenesulphonate) (PEDOT:PSS)-covered indium tin oxide (ITO) glass in the sequence PbI_2 then MAI. Since PbI_2 has relatively low solubility in 2-propanol, the spin-coating of MAI did not wash off the PbI_2. Our previous studies showed that the interdiffusion method can form continuous, compact perovskite films; details of the perovskite film formation can be found in the Methods section. The thickness of the perovskite films was controlled from 160 to 1015 nm by changing the concentration of precursors. The stacking films were then annealed at a temperature of 100 °C with or without DMF vapor for 1 h. The films without solvent annealing only went through thermal annealing and were used as control samples. Since both PbI_2 and MAI have high solubility in DMF, the DMF vapor provided a wet environment so that the precursor ions and molecules could diffuse a longer distance than in all solid-state thermal annealing, which promotes the grain growth and yields a larger grain size, as illustrated in Figure 1b,c.

Figure 2 shows the scanning electron microscopy (SEM) top surface images of perovskite films with thicknesses of 250, 430, and 1015 nm, respectively, with and without solvent annealing. Their in-plane grain size distributions are shown on the right side of the SEM images. The film thicknesses are also marked as black vertical dashed lines in the grain size histograms. The following conclusions can be drawn from the SEM study. First, all of the films with and without solvent annealing follow a normal grain growth mode where the average grain size increases uniformly in all directions.[25] Second, the grain

Z. Xiao, Dr. Q. Dong, C. Bi, Y. Shao, Dr. Y. Yuan, Prof. J. Huang
Department of Mechanical and Materials Engineering and Nebraska Center for Materials and Nanoscience
University of Nebraska-Lincoln
Lincoln, NE 68588–0526, USA
E-mail: jhuang2@unl.edu

DOI: 10.1002/adma.201401685

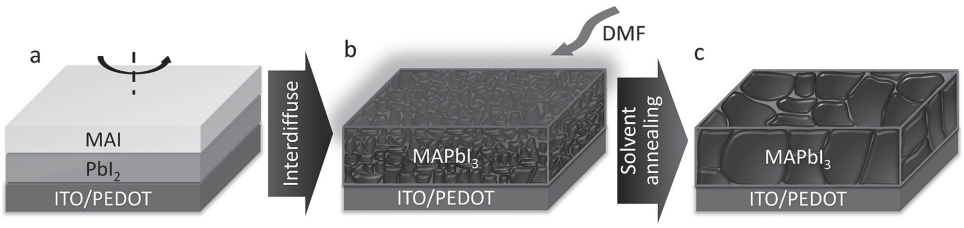

Figure 1. Schematics of the interdiffusion approach and solvent-annealing-induced grain size increase.

size of the solvent-annealed films increases almost linearly with the film thickness up to 1015 nm, while the maximum grain size in the thermally annealed films remains around 260 nm irrespective of film thickness. Third, the average grain sizes of the solvent-annealed films are always slightly larger or comparable to the film thicknesses, which should greatly enhance the

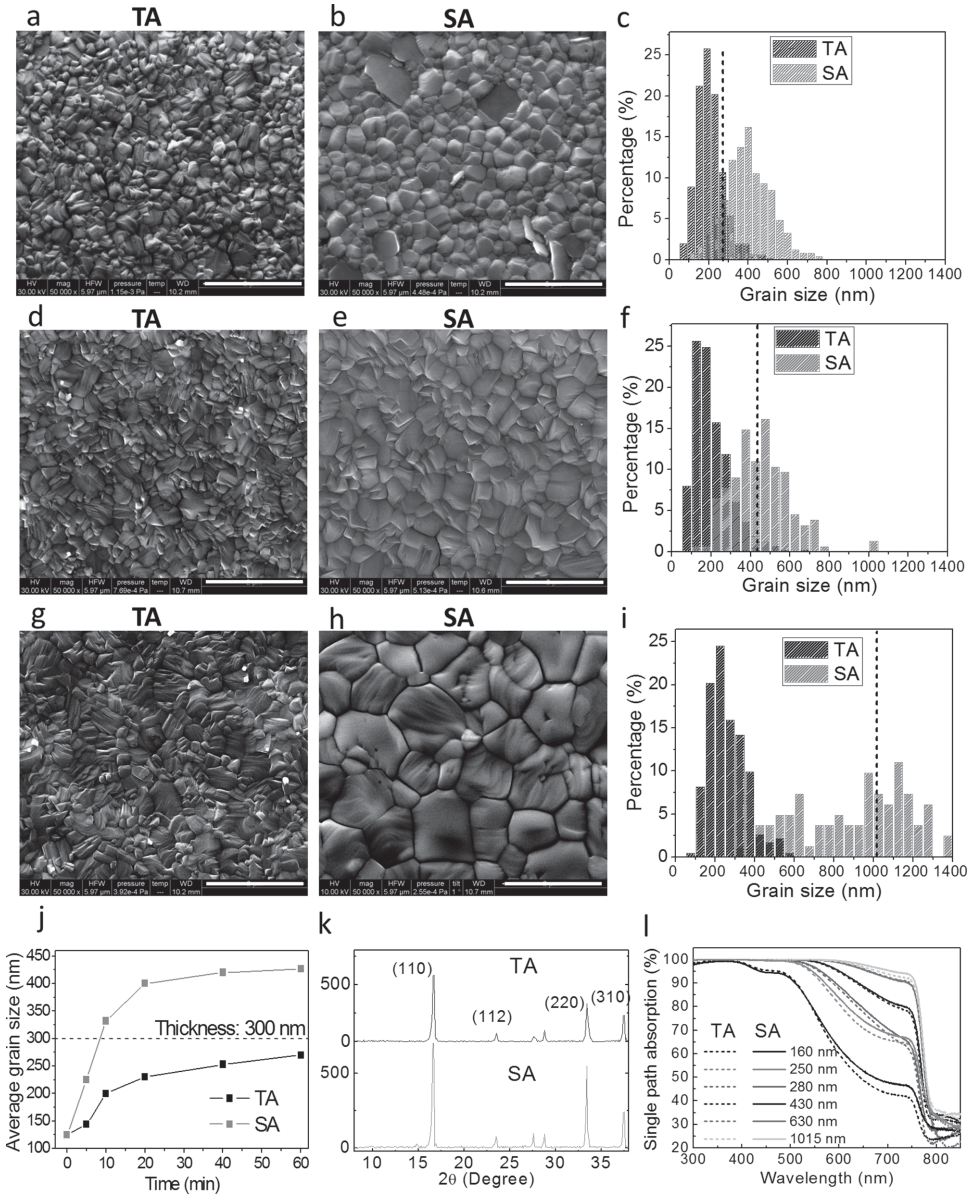

Figure 2. SEM images of the thermally annealed (TA) perovskite films with thicknesses of 250 nm (a), 430 nm (d), and 1015 nm (g), and solvent-annealed (SA) perovskite films with thickness of 250 nm (b), 430 nm (e) and 1015 nm (h); the scale bars in the SEM micrographs are 2 μm. c,f,i) Grain-size distributions of the SEM images to the left. j) Average grain size versus annealing time for the 300 nm thick perovskite films. k) XRD patterns of the thermally annealed and solvent-annealed 300 nm thickness perovskite films. l) Single-path absorption of the perovskite films with different thicknesses.

Adv. Mater. **2014**,
DOI: 10.1002/adma.201401685

charge extraction process; this is because the photogenerated charges do not need to go through any grain boundaries during their transport in the out-of-plane direction before being collected by the electrodes.

The dynamic grain growth process of thermal annealing and solvent annealing of a 300 nm thick perovskite films was studied by varying thermal and solvent annealing time from 0 to 60 min. The SEM surface images are shown in Figure S1 in the Supporting Information. The average grain size versus time is summarized in Figure 2j. Due to the quick reaction of PbI_2 and MAI and quick crystallization of $MAPbI_3$, the as-prepared perovskite films were polycrystalline with a small average grain size of 125 nm. The grain size of both thermally annealed and solvent-annealed films grew with increased annealing time. The grain size increase was fast in the first 20 min, and then slowed down and saturated with further annealing. The grain size of the solvent-annealed film grew much faster than the thermally annealed films: solvent-annealing for 20 min increased the average grain size to 400 nm, which was already larger than the film thickness, while thermal-annealing for 60 min only increased the grain size to 260 nm, smaller than the film thickness.

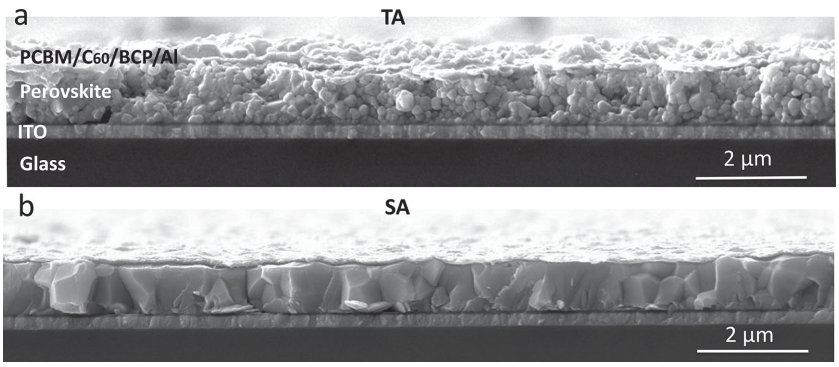

Figure 3. Cross-sectional SEM images of the thermally annealed (a) and solvent-annealed (b) perovskite films with thickness 1015 nm.

The solvent annealing-induced crystallinity change was measured by X-ray diffraction (XRD). Figure 2k shows the XRD results of the solvent-annealed and thermally annealed 300 nm thick perovskite films. All of the XRD diffraction peaks of the solvent-annealed films were sharper than those of the thermal-annealed films, which indicates increased crystallinity with fewer low-dimensional defects and/or larger grain size with less scattering of grain boundaries. The relative intensity of the diffraction peaks from the different planes did not change, indicating that the grain crystal orientation of the solvent-annealed film should not change during the solvent annealing process. The absorption spectra of the perovskite films with different thicknesses were also measured, and the result is shown in Figure 2l. The increased band-edge absorption, around 750 nm, should be due to the improved crystallinity and/or the full reaction of precursors under the facilitation of DMF vapor.

Hall effect measurements were conducted on the 300 nm thick films to determine the morphology-correlated electric property change. The results showed that all of the perovskite films were p-type. After solvent annealing, the hole mobility increased from 30 to 45 $cm^2\ V^{-1}\ s^{-1}$; and the extrinsic hole concentration decreased from 1.8×10^{14} to 6.2×10^{13} cm^{-3}. Both variations can be ascribed to the larger grains with better crystallinity and decreased grain boundary density in the solvent-annealed films.

Photovoltaic devices were fabricated to evaluate the influence of improved crystallinity and enlarged grain size on device performance. The devices were structured ITO/PEDOT:PSS/$MAPbI_3$/[6,6]-phenyl-C61-butyric acid methyl ester (PCBM) (10 nm)/C_{60} (20 nm)/2,9-dimethyl-4,7-diphenyl-1,10-phenanthroline (BCP) (8 nm)/aluminium (Al) (100 nm). The device area was 9.6 mm^2, determined by the overlap of the cathode and anode. In order to avoid the overestimation of the photocurrent density by the optical piping effect, an aperture size of 8 mm^2 was used to define the light absorption area. Double fullerene layers were used, because they can passivate the defects with different depths at both the perovskite surface and the grain boundaries in a complementary way.[26,27] **Figure 3** shows the SEM cross-sectional images of the thermally annealed and solvent-annealed devices with a perovskite layer thickness around 1015 nm. As one can see, the grains in the thermally annealed device are smaller than the film thickness, while the grains in the solvent-annealed film are so large that a single grain can connect the cathode and anode. It can be inferred that, in the solvent-annealed perovskite devices, most of the photogenerated charges can reach the electrodes without encountering grain boundaries, which should significantly reduce charge loss by recombination at grain boundaries in thick perovskite film devices.

Figure 4a–h show the photocurrent curves as well as the external quantum efficiency (EQE) of the device with perovskite thickness from 160 to 1015 nm; the devices' performance are shown in Table S2 in the Supporting Information. When the perovskite film is thinner than 300 nm, which is comparable to the grain size of both thermally annealed and solvent-annealed perovskite films, the photogenerated carriers are expected to be effectively extracted out without severe recombination, since there would be fewer grain boundaries along the charge transportation paths. In this case, the photocurrent of the solvent-annealed devices had only slightly higher photocurrent than the thermally annealed devices. The J_{SC} of 16–17 mA cm^{-2} from the 160 nm thick perovskite film devices were relatively small because of insufficient absorption in the red spectrum region. The J_{SC} of the solvent-annealed device kept increasing with the thickness due to stronger absorption, evidenced by the dramatically increased EQE in the 550–800 nm spectral range. It reached a maximum value of 21.1 mA cm^{-2} in the devices with a perovskite film thickness of 630 nm. For the thermal-annealed devices, the J_{SC} and *FF* increased slightly with an increased perovskite film thickness to 300 nm. However, the J_{SC} and *FF* of the thermally annealed devices decreased when the thickness of the perovskite films was further increased to surpass the invariable grain size. It is deduced that the charge recombination at these grain boundaries severely reduced the device performance. If all of the photogenerated charges were collected by the diffusion of charges to electrodes, the charge

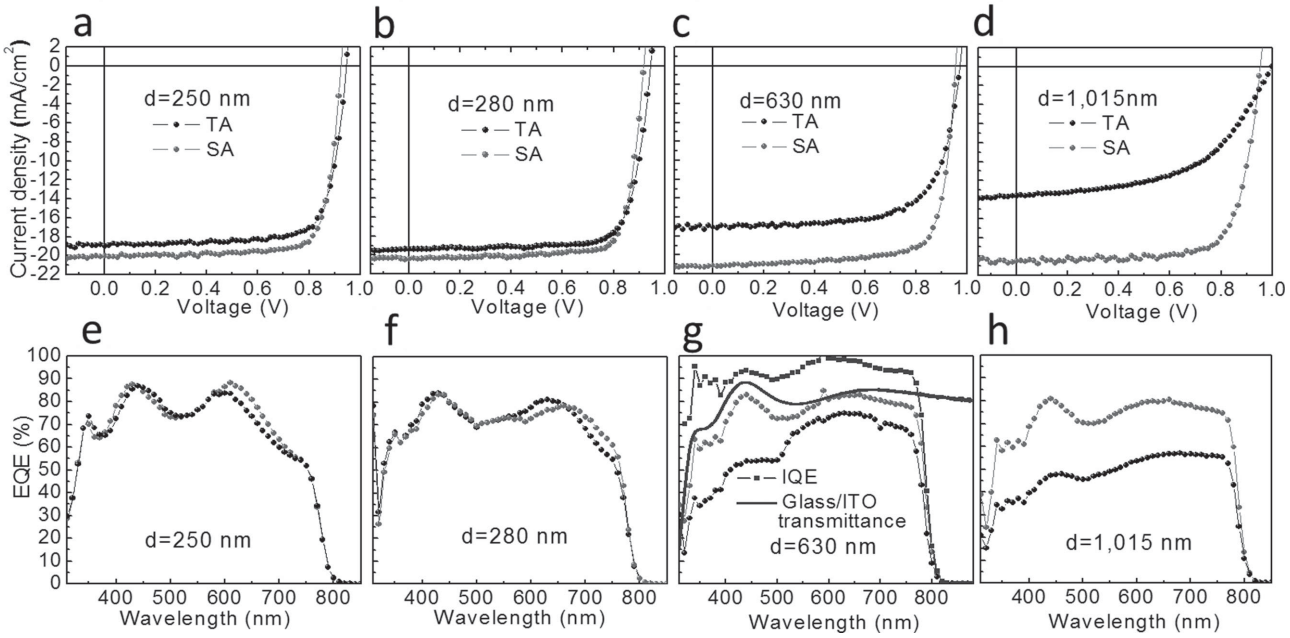

Figure 4. Photocurrent characteristics (a–d) of the perovskite devices with film thickness of 250, 300, 630, and 1015 nm, respectively. e–h) EQE of the perovskite devices with film thicknesses. Black circles: thermal annealing; gray circles: solvent annealing.

diffusion length of the solvent-annealed perovskite films would be larger than 1 μm, much longer than the thermally annealed film of around 300 nm. According to the solvent annealing working principle, any solvent with large solubility to MAI and PbI_2 should also work well for solvent annealing. Dimethyl sulfoxide (DMSO) was also tested, which verified this scenario. The PCE of a 630 nm thick devices was increased from 9.9% to 15.6% by using DMSO as the solvent for annealing, as shown in Figure S2 in the Supporting Information. This result proves that the solvent annealing approach is universal.

It is noted that all of the solvent-annealed devices had large *FF* of around 75–80%. This can be understood by the fact that the average grain size of the solvent-annealed film was always larger than the thickness of the film, so that the charges could transport and be collected through a single grain without encountering grain boundaries. The device efficiency of the solvent-annealed perovskite solar cells with different thicknesses stayed above 14.5% with the thickness varied from 250 to 1015 nm.

There is an obvious trend in that the EQE spectra near the absorption edge increases and the whole spectra becomes more flat as the thickness of the film increases. This is due to the increased single path absorption of the thicker perovskite films. As shown in Figure 2l, the single path absorption reached above 90% across the whole absorption spectrum when the perovskite film was thicker than 630 nm. The average EQE reached 83% for the 630 nm thick devices. The trough of EQE at around 520 nm was caused by the reflection of the glass/ITO substrate, as shown in Figure 4g. Assuming all of the light transmitted through ITO/glass was absorbed by the perovskite films, the internal quantum efficiency (IQE), calculated by dividing the EQE with the transmittance, of the 630 nm thick device reached 95% on average, with the peak IQE reaching 100% at around 600 nm (Figure 4g). This indicates that the limitation on further photocurrent enhancement is the reflection of incident sunlight by the glass/ITO or other interfaces of the perovskite devices. It is thus expected that J_{SC} can be further increased to 25.0 mA cm^{-2} by applying an antireflective coating.

Since the photocurrent hysteresis was shown to be a major issue in accurate characterization of device efficiency, we measured a solvent-annealed high-efficiency device by changing the scanning directions and scanning rates. No photocurrent hysteresis was observed with different scanning rates or scanning directions. In order to verify the measured efficiency is right, we measured steady-state photocurrent output at the maximum power point (0.82 V). The steady-state photocurrent represents the actual power output and should be used to accurately characterize the device efficiency. As shown in **Figure 5**c, the photocurrent rose quickly to maximum, and the steady-state current is the same as that measured from the photocurrent scanning. The photocurrent was stable.

In order to determine the origin of the efficiency enhancement of the solvent-annealed devices, we used thermal admittance spectroscopy (TAS) to measure trap density of states (*t*DOS) reduction induced by increased crystallinity and grain size. The 1015 nm thick perovskite devices were used for this study. TAS is an established and effective technique to measure the trap density in thin-film solar cells.[28,29] The experiment details and calculations of the *t*DOS can be found in the Methods section. As shown in **Figure 6**a, the *t*DOS of the solvent-annealed device was 2–7 times smaller than the thermal-annealed device. The measured surface trap density is in the same order of magnitude as that derived from a photoluminescence lifetime study.[30] It has been established in another of our studies that the charge traps in this energy band originate from the grain boundary by the fact that the diffusion of fullerene into the grain boundaries effectively reduce the trap

Adv. Mater. **2014**,
DOI: 10.1002/adma.201401685

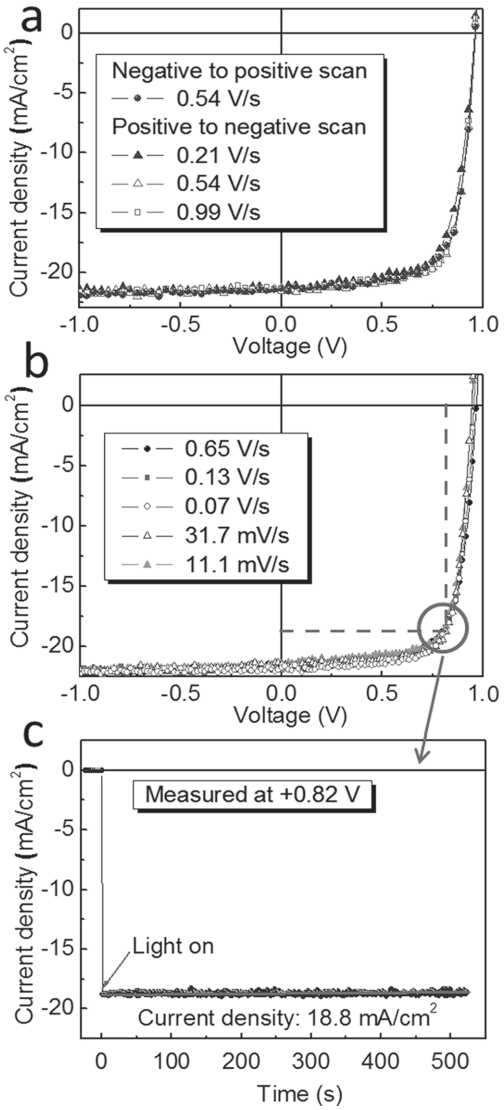

Figure 5. Photocurrent curves of a best performing device with: a) different scanning directions, and b) different scanning rates measured from negative to positive bias. c) Steady-state photocurrent output at the maximum power point (0.82 V).

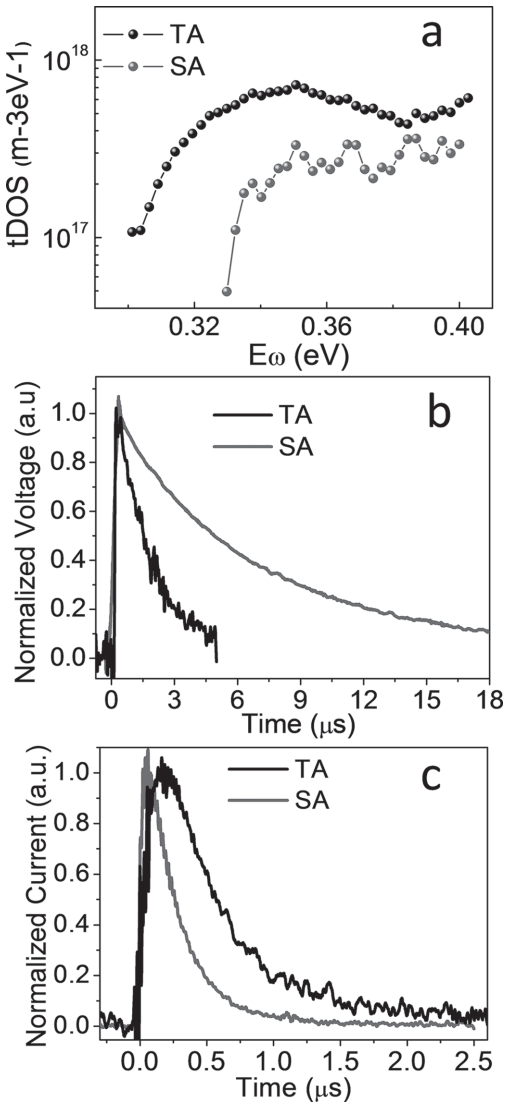

Figure 6. a) Trap density of states calculated from the thermal admittance spectroscopy measurement. b) Photovoltage decay under 0.3 Sun illumination measured by TPV. c) Photocurrent decay measured by TPC.

density in this band.[27] The total trap density, calculated by integrating the *t*DOS in this band, of the solvent-annealed device is 1.8×10^{16} m^{-3} which is three-times smaller than that of the thermally annealed device (5.3×10^{16} m^{-3}). If the grain boundary has same density of traps in both films, the total trap density of the solvent-annealed film should be 16-times smaller than in the thermally annealed film because the grain size is four-times larger. This indicates the nature of the grain boundaries in both types of films is different, and it is possible that fullerene can diffuse further in the thermally-annealed films along the grain boundaries to passivate the traps. As shown in Figure 3a and b, the grains of the solvent-annealed film are more compact so that it is harder for the fullerene to diffuse. This result clearly verifies that the charge trap density is dramatically reduced by the much smaller total grain boundary areas in the solvent-annealed films, which have much larger grain size.

In order to examine the effect of the reduced *t*DOS on the performance of the device, the charge-recombination lifetime and charge-extraction time were measured by transient photovoltage (TPV) and transient photocurrent (TPC) techniques, respectively.[31] As shown in Figure 6b, the charge-recombination lifetime of the solvent-annealed device was increased to 7.2 μs, compared to 1.7 μs in the thermally annealed device, under 0.3 Sun illumination at open-circuit voltage condition. We also measured the device under illumination using impedance spectroscopy and derived the charge-recombination lifetime, which yielded results consistent with TPV measurements. The reduced trap density also resulted in larger carrier mobility, which further resulted in quicker charge extraction. As shown in Figure 6c, the charge-extraction time measured at zero bias decreased to 0.25 μs for the solvent-annealed device, compared with 0.57 μs for the thermally annealed device, which

corresponds to an increase of transit mobility by 2.3 times. The rising time of the photocurrent of the thermally annealed device was longer than that of the solvent-annealed device, which also demonstrates the higher trap density in the thermally annealed device. It is noted that the ratio of Hall mobility increase (1.5 times) is smaller than the transit mobility increase. This might be due to the Hall mobility measuring the in-plane conduction of the carriers, and the TPC measures carrier transportation along the out-of-plane direction, while the grain structures in these two directions are different. Nevertheless, there is a disparity of carrier mobilities measured by these two methods, which is not understood yet. The charge-carrier diffusion length was estimated by the diffusivity (D) and carrier lifetime. The diffusivity was calculated from the drift mobility measured by TPC using the Einstein relationship: $D = \frac{\mu k_B T}{e}$, where μ is the drift mobility, k_B is Boltzmann's constant and T is the absolute temperature. The carrier lifetime was estimated from the TPV measurement, which gives the low limit of the charge recombination lifetime because the carrier concentration at V_{OC} is larger than time-resolved photoluminescence measurement due to the charge injection. The calculated carrier diffusion length of the solvent-annealed device is 886 nm, which is close to the maximum film thickness, and around four times longer than that in the thermal annealed devices of 282 nm. All these facts—including increased charge recombination lifetime, decreased charge extraction time, and increased carrier diffusion length—can be ascribed to the increased grain size and crystallinity of the perovskite films by solvent annealing.

In summary, solvent annealing was first reported to be an effective method to increase the organolead triiodine perovskite grain size and crystallinity, which resulted in significant material electronic property improvement and performance enhancement of the photovoltaic devices. The effective charge diffusion length of the solvent-annealed $MAPbI_3$ films was increased to longer than 1 μm, much longer than the previously reported 300 nm. The highest device efficiency reached 15.6%, and device efficiency stayed above 14.5% as the perovskite thickness increased to 1015 nm.

Experimental Section

Perovskite Film Fabrication and Characterization: Methylammonium iodide (CH_3NH_3I, MAI) was synthesized using the method described by Lee et al.[8] PbI_2 (dissolved in DMF, with different concentrations) was spin-coated on top of PEDOT:PSS/ITO substrate at 6000 rpm for 35 s. Then MAI (dissolved in 2-propanol at different concentrations) was spin-coated on top of the dried PbI_2 layer at room temperature at 6000 rpm for 35 s. More details of the perovskite film fabrication can be found in the Supporting Information. All of the films were solvent- or thermally annealed at 100 °C for 1 h.

For the film treated with solvent annealing, the perovskite films were put on top of a hot plate and covered by a glass petri dish. Around 10 μL of DMF solvent was added at the edge of the petri dish during the thermal-annealing process, so that the DMF vapor could go into the Petri dish and make contact with the perovskite layer. The DMF vapor was expected to be able to penetrate into the perovskite film and help the growth of crystalline domains.

XRD measurements were performed with a Rigaku D/Max-B X-ray diffractometer with Bragg–Brentano parafocusing geometry, a diffracted beam monochromator, and a conventional cobalt target X-ray tube set to 40 kV and 30 mA. The single-path absorption was measured using an Evolution 201 UV–Visible spectrometer (Thermo Scientific). A Quanta 200 FEG environmental scanning electron microscope (ESEM) using a field-emission gun (FEG) electron source was used to scan the surface and cross-sectional film morphology. The films were first covered with a thin layer of gold, coated using a Cressington 108 Auto Sputter Coater, before the SEM measurement.

Device Fabrication and Characterization: For the device using the interdiffusion process, the PCBM (dissolved in DCB, 2 wt%) was spin-coated on top of the perovskite layer at 6000 rpm for 35 s. Then the films were annealed at 100 °C for 60 min. The device was finished by thermal evaporation of C_{60} (20 nm), BCP (8 nm), and Al (100 nm).

The steady-state photocurrent curves were measured under simulated AM 1.5G irradiation (100 mW cm^{-2}) using a xenon-lamp-based solar simulator (Oriel 67005, 150 W Solar Simulator). The scanning rate for the *I–V* curve was 0.13 V s^{-1}, excluding those marked specifically. For each measurement, the lamp was turned on and the testing started 30 min later. A Schott visible-color, glass-filtered (KG5 color-filtered) Si diode (Hamamatsu S1133) was used to calibrate the light intensity before the photocurrent measurement. We used a Keithley 2400 Source-Meter for the *I–V* measurement. EQE was measured with a Newport QE measurement kit by focusing a monochromatic beam of light onto the devices.

Impedance spectroscopy was measured by an LCR Meter (Agilent E4980A). The trap density of states was derived from the angle frequency dependent capacitance using the equation: $N_T(E_\omega) = -\frac{V_{bi}}{qW}\frac{dC}{d\omega}\frac{\omega}{k_B T}$, where C is the capacitance, ω is the angular frequency, q is the elementary charge, k_B is the Boltzmann's constant, and T is the absolute temperature. V_{bi} and W, extracted from capacitance–voltage measurements, are the built-in potential and depletion width, respectively. The applied angular frequency ω defines an energetic demarcation, $E_\omega = k_B T \ln\left(\frac{\omega_0}{\omega}\right)$, where ω_0 is the attempt-to-escape frequency. The trap states above the energy demarcation cannot contribute to the capacitance due to their slow rate to capture or emit charges.

Transient Photovoltage (TPV) and Transient Photocurrent (TPC) Measurements: The device was serially connected to a digital oscilloscope (DOS-X 3104A) and the input impedance of the oscilloscope set to 1 MΩ and 50 Ω, respectively, to form the open- and short-circuit conditions, respectively, for monitoring the charge density decay and charge extraction time. The TPV was measured under 0.3 Sun illumination. An attenuated UV laser pulse (SRS NL 100 Nitrogen Laser) was used as a small perturbation to the background illumination on the device. The laser-pulse-induced photovoltage variation (ΔV) was smaller than 5% of the V_{OC} produced by the background illumination. The wavelength of the N_2 laser was 337 nm, the repeating frequency was ca. 10 Hz, and the pulse width was less than 3.5 ns.

Supporting Information

Supporting Information is available from the Wiley Online Library or from the author.

Acknowledgements

The authors thank financial support from the Department of Energy under Award DE-EE0006709 and the Defense Threat Reduction Agency under award HDTRA1-14-1-0030.

Received: April 14, 2014
Revised: July 1, 2014
Published online:

[1] G. Li, V. Shrotriya, J. Huang, Y. Yao, T. Moriarty, K. Emery, Y. Yang, *Nat. Mater.* **2005**, *4*, 864.

DOI: 10.1002/adma.201401685

[2] X. Liu, H. Wang, T. Yang, W. Zhang, X. Gong, *ACS Appl. Mater. Interfaces* **2012**, *4*, 3701.
[3] G. Li, Y. Yao, H. Yang, V. Shrotriya, G. Yang, Y. Yang, *Adv. Funct. Mater.* **2007**, *17*, 1636.
[4] Q. Chen, H. Zhou, Z. Hong, S. Luo, H.-S. Duan, H.-H. Wang, Y. Liu, G. Li, Y. Yang, *J. Am. Chem. Soc.* **2013**, *136*, 622.
[5] J. Burschka, N. Pellet, S.-J. Moon, R. Humphry-Baker, P. Gao, M. K. Nazeeruddin, M. Grätzel, *Nature* **2013**, *499*, 316.
[6] M. Liu, M. B. Johnston, H. J. Snaith, *Nature* **2013**, *501*, 395.
[7] A. Kojima, K. Teshima, Y. Shirai, T. Miyasaka, *J. Am. Chem. Soc.* **2009**, *131*, 6050.
[8] M. M. Lee, J. Teuscher, T. Miyasaka, T. N. Murakami, H. J. Snaith, *Science* **2012**, *338*, 643.
[9] A. Abrusci, S. D. Stranks, P. Docampo, H.-L. Yip, A. K. Y. Jen, H. J. Snaith, *Nano Lett.* **2013**, *13*, 3124.
[10] J. M. Ball, M. M. Lee, A. Hey, H. J. Snaith, *Energy Environ. Sci.* **2013**, *6*, 1739.
[11] G. Hodes, *Science* **2013**, *342*, 317.
[12] J. Y. Jeng, Y. F. Chiang, M. H. Lee, S. R. Peng, T. F. Guo, P. Chen, T. C. Wen, *Adv. Mater.* **2013**, *25*, 3727.
[13] H.-S. Kim, I. Mora-Sero, V. Gonzalez-Pedro, F. Fabregat-Santiago, E. J. Juarez-Perez, N.-G. Park, J. Bisquert, *Nat. Commun.* **2013**, *4*, 2242.
[14] H. J. Snaith, *J. Phys.Chem. Lett.* **2013**, *4*, 3623.
[15] S. D. Stranks, G. E. Eperon, G. Grancini, C. Menelaou, M. J. Alcocer, T. Leijtens, L. M. Herz, A. Petrozza, H. J. Snaith, *Science* **2013**, *342*, 341.
[16] W. Zhang, M. Saliba, S. D. Stranks, Y. Sun, X. Shi, U. Wiesner, H. J. Snaith, *Nano Lett.* **2013**, *13*, 4505.
[17] G. Xing, N. Mathews, S. Sun, S. S. Lim, Y. M. Lam, M. Grätzel, S. Mhaisalkar, T. C. Sum, *Science* **2013**, *342*, 344.
[18] J. H. Heo, S. H. Im, J. H. Noh, T. N. Mandal, C.-S. Lim, J. A. Chang, Y. H. Lee, H.-j. Kim, A. Sarkar, M. K. Nazeeruddin, *Nat. Photonics* **2013**, *7*, 486.
[19] P. Docampo, J. M. Ball, M. Darwich, G. E. Eperon, H. J. Snaith, *Nat. Commun.* **2013**, *4*, 2761.
[20] E. Edri, S. Kirmayer, A. Henning, S. Mukhopadhyay, K. Gartsman, Y. Rosenwaks, G. Hodes, D. Cahen, *Nano Lett.* **2014**,*14*, 1000.
[21] C. E. Small, S. W. Tsang, S. Chen, S. Baek, C. M. Amb, J. Subbiah, J. R. Reynolds, F. So, *Adv. Energ. Mater.* **2013**, *3*, 909.
[22] A. Dualeh, N. Tétreault, T. Moehl, P. Gao, M. K. Nazeeruddin, M. Grätzel, *Adv. Funct. Mater.* **2014**, *24*, 3250.
[23] C. Bi, Y. Shao, Y. Yuan, Z. Xiao, C. Wang, Y. Gao, J. Huang, unpublished.
[24] Z. Xiao, C. Bi, Y. Shao, Q. Dong, Q. Wang, C. Wang, Y. Gao, J. Huang, *Energy Environ. Sci.* **2014**, *7*, 2619.
[25] C. Thompson, *Ann. Rev. Mater. Sci.* **2000**, *30*, 159.
[26] Q. Wang, Y. Shao, Q. Dong, Z. Xiao, Y. Yuan, J. Huang, *Energy Environ. Sci.* **2014**, *7*, 2359.
[27] Y. Shao, Z. Xiao, Q. Wang, Y. Gao, J. Huang, unpublished.
[28] T. Walter, R. Herberholz, C. Müller, H. Schock, *J. Appl. Phys.* **1996**, *80*, 4411.
[29] *Advanced Characterization Techniques for Thin Film Solar Cells*, (Eds: U. Rau, D. Abou-Ras, T. Kirchartz), Wiley, Weinheim, Germany, **2011**.
[30] G. Xing, N. Mathews, S. S. Lim, N. Yantara, X. Liu, D. Sabba, M. Grätzel, S. Mhaisalkar, T. C. Sum, *Nat. Mater.* **2014**, *13*, 476.
[31] C. Shuttle, B. ORegan, A. Ballantyne, J. Nelson, D. Bradley, J. De Mello, J. Durrant, *Appl. Phys. Lett.* **2008**, *92*, 093311.